ADVANCED MATERIALS
www.advmat.de

Current Control of Spin Helicity and Nonreciprocal Charge Transport in a Multiferroic Conductor

Daiki Yamaguchi, Aki Kitaori, Naoto Nagaosa, and Yoshinori Tokura**

A multiferroic state with both electronic polarity (*P*) and magnetization (*M*) shows the inherently strong *P*-*M* coupling when *P* is induced by cycloidal (Néel-wall like) spin modulation. The sign of *P* is determined by the clockwise or counterclockwise rotation of spin, termed the spin helicity. Such a multiferroic state is not limited to magnetic insulators but can be broadly observed in conductors. Here, the current control of the multiferroics is reported in a helimagnetic metal YMn_6Sn_6 and its detection through nonreciprocal resistivity (NRR). The underlying concept is the coupling of the current with the toroidal moment $T \sim P \times M \sim (\hat{q} \times \chi_\nu) \times M$ as well as with the magneto-chirality $\chi_\nu \cdot M$, where $\hat{q}$ and χ_ν are the unit modulation wave vector and the vector spin chirality, respectively. An enhancement of NRR is furthermore observed by the spin-cluster scattering via χ_ν and its fluctuation. These findings may pave the way to an exploration of multiferroic conductors and the application of the spin-helicity degree of freedom as a state variable.

1. Introduction

The chirality is one of the fundamental notions in a broad field of science. In condensed matter science, chirality in magnetism has been attracting enormous interest in terms of multiferroics, skyrmions, nonreciprocal responses, and their application to spintronic devices. For example, the chirality can be found in helical magnetic structures, such as a proper screw or Bloch-wall-like (**Figure 1E**) and cycloidal or Néel-wall like (Figure 1G (plan view)) spin states. Here, the term *spin helicity* refers to the rotation sense of spins in proceeding along the modulation wave vector $\boldsymbol{q}$. The spin helicity in helimagnetic structures is reversed by a mirror operation.

Multiferroics are the materials, in which multiple ferroic orders, such as ferroelectricity, ferroelasticity, and ferromagnetism, coexist.[1] In particular, the coupling of ferroelectricity and ferromagnetism/antiferromagnetism has been intensively studied in the last few decades. In insulating multiferroics, the mutual control of magnetization ($\boldsymbol{M}$) and electric polarization ($\boldsymbol{P}_e$) by electric and magnetic fields, respectively, is realized via the magnetoelectric (ME) effect. Multiferroics of spin origin can emerge in some helical magnetic structures with a spin-helicity degree of freedom. A microscopic mechanism to generate the $\boldsymbol{P}_e$ or more generally the electronic polarity ($\boldsymbol{P}$) including metallic case, from noncollinear spin modulation has been proposed, termed the spin current model,[2] or inverse Dzyaloshinskii-Moriya model.[3,4] In this model, the emerging $\boldsymbol{P}$ is expressed as

$$\boldsymbol{P} = A \sum \boldsymbol{e}_{ij} \times \boldsymbol{\chi}_\nu^{ij} = A \sum \boldsymbol{e}_{ij} \times \left(\boldsymbol{S}_i \times \boldsymbol{S}_j\right) \quad (1)$$

where A is a coupling constant that reflects the spin exchange interaction and spin-orbit coupling (SOC), and $\boldsymbol{e}_{ij}$ is the unit vector connecting neighboring-site spins $\boldsymbol{S}_i$ and $\boldsymbol{S}_j$. $\boldsymbol{\chi}_\nu^{ij} = \boldsymbol{S}_i \times \boldsymbol{S}_j$ is the vector spin chirality. This formula ensures that the canting modulation of spins produces the local $\boldsymbol{P}$. The local $\boldsymbol{P}$ remains macroscopically finite in some helimagnetic structures such as the cycloidal spin structure (Figure 1G (plan view)). In the cycloidal spin structure, the neighboring-site spins are stabilized at an angle in the spin rotation plane, which is parallel to the modulation direction ($\boldsymbol{q}$ vector). (In the case of constant-pitch helical spins, the vector spin chirality χ_ν takes a value independent of site pair ij.) This mechanism has been experimentally confirmed in various magnetic insulators.[1] The direction of $\boldsymbol{P}$ depends on the spin helicity of cycloid, i.e., the direction of cycloidal spin rotation. It is demonstrated that the spin-helicity control by the electric and magnetic fields switches the direction of $\boldsymbol{P}_e$ in multiferroic (Mott) insulators.[5,6] One of the motivations of the

D. Yamaguchi, A. Kitaori, Y. Tokura
Department of Applied Physics
The University of Tokyo
Tokyo 113–8656, Japan
E-mail: dai.20.yama.011-1@g.ecc.u-tokyo.ac.jp; tokura@riken.jp
D. Yamaguchi, N. Nagaosa, Y. Tokura
RIKEN Center for Emergent Matter Science (CEMS)
Wako 351-0198, Japan
A. Kitaori
Institute of Engineering Innovation
The University of Tokyo
Tokyo 113-0032, Japan
N. Nagaosa
Fundamental Quantum Science Program
TRIP Headquarters, RIKEN
Wako 351-0198, Japan
Y. Tokura
Tokyo College
The University of Tokyo
Tokyo 113–8656, Japan

The ORCID identification number(s) for the author(s) of this article can be found under https://doi.org/10.1002/adma.202420614

DOI: 10.1002/adma.202420614

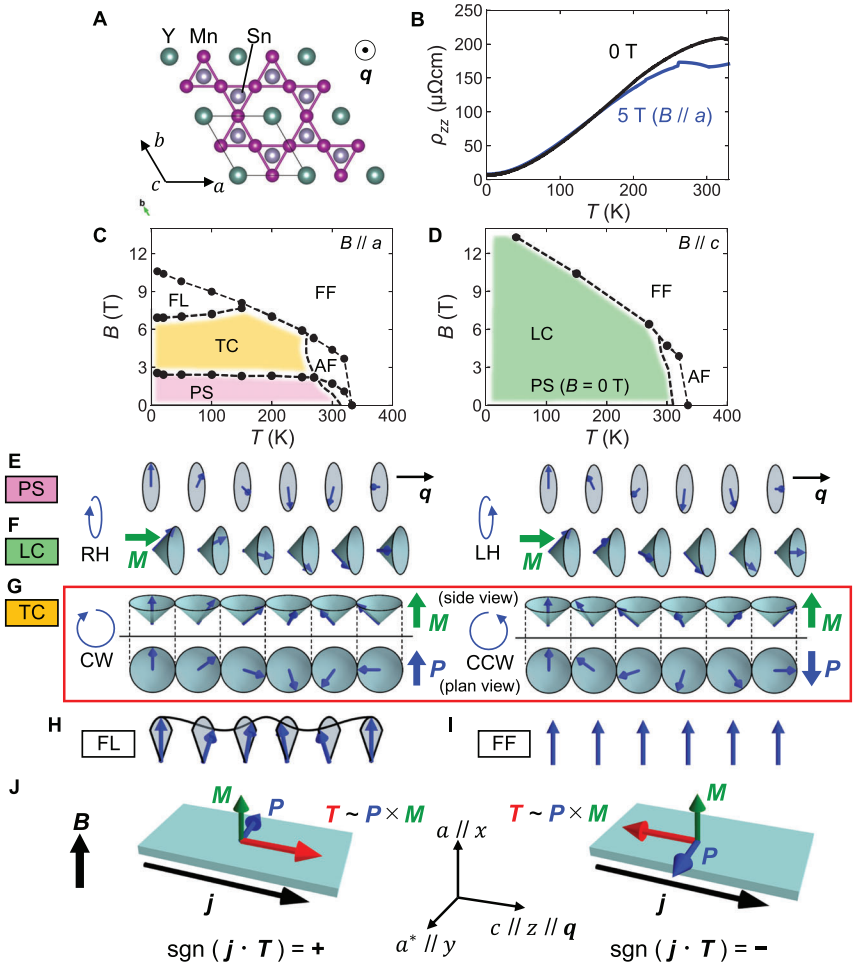

Figure 1. Crystal and magnetic structures of YMn_6Sn_6 with the definition of spin helicity. A) Schematic crystal structure of YMn_6Sn_6 viewed along the *c*-axis, drawn by using VESTA.[38] B) Temperature dependence of longitudinal resistivity along the *c*-axis in 0 T (black) and 5 T (***B***//*a*) (blue). Magnetic phase diagram of YMn_6Sn_6 with C) ***B***//*a* and D) ***B***//*c*. PS, LC, TC, AF, FL, and FF stand for proper screw, longitudinal conical, transverse conical, antiferromagnetic, fan like, and forcedly ferromagnetic structures, respectively. The black points representing the phase boundaries in (C) and (D) are obtained by magneto-transport measurements in this study. The phase boundary of AF phase is taken from the literature.[23] Schematics of E) PS and F) LC structures. PS and LC of opposite spin helicities, i.e., right-handed (RH) and left-handed (LH) screws are shown. G) Schematic of TC structure. Upper and lower show the side and plan views of TC structure, respectively. Clockwise (CW) and counterclockwise (CCW) spin helicities are shown. Schematics of H) FL and I) FF structures, where spin helicity is not defined. J) Direction of toroidal moment ***T*** (red arrows) for CW and CCW modulations. The black arrow indicates the electric current *j* along the ***q*** vector. The light-blue plate represents the sample. TC phase is stabilized by the application of external magnetic field ***B***//*a*. The direction of spontaneous magnetization ***M*** and electronic polarity ***P*** are indicated by green and blue arrows in (F) and (G).

present work is to test the generation of the electronic polarity (***P***) even in a conductor with the cycloidal spin state and its control in analogy to the multiferroic insulators. The term "electric polarization" is established for insulators, but is generally not well-defined for conductors. Here, we define the counterpart for conductors as *electronic polarity*, since the concept of "polar metal" can be regarded as established (see also Section S5, Supporting Information).[7,8] The conventional term *multiferroics* have traditionally referred to the coexistence of (anti)ferromagnetic order and ferroelectric order (or permanent polarization $\boldsymbol{P}_e$). In this study, we extend the concept of multiferroics to include materials where time-reversal and space-inversion symmetries are simultaneously broken, such as in cases where ferromagnetic order coexists with electronic polarity ***P*** originating from spin. A key feature of such generalized multiferroics is the emergence of the toroidal moment ***T*** or the toroidal order with ***T*** as an order parameter. The electric-field control of ***P*** (or spin helicity) appears impossible in a conductor because of strong metallic screening, and instead, we try to exploit ***T***, which can couple with the flowing current in conducting multiferroics.[9] The counterpart concept of ME effect in multiferroic conductors is hereafter termed *magnetopolar* (MP) *effect*, in which "polar" refers to the direction of the electronic polarity, not the electric polarization, which can be controlled by the application of electric current instead of the electric field. We will define the two kinds of MP effect, i.e., the electrical magnetochiral effect (eMChE) and *electrical magneto-toroidal effect* (eMToE), as elucidated below.

Helimagnets have recently been attracting attention in terms of the spintronic application for a novel magnetic memory or computing device.[10–12] For example, the spin-helicity degree of freedom in helimagnets has the potential as a state variable. To this end, the spin helicity should be controlled and detected electrically in conducting helimagnets. This was recently successfully achieved in a centrosymmetric itinerant proper-screw helimagnet MnP,[11] followed by the demonstration of the spin-helicity control for proper-screw $MnAu_2$ thin film at room temperature.[12] In these cases, the electrical magnetochiral effect (eMChE) was used to control and detect the spin helicity.[13–15] The control parameter for eMChE is $\boldsymbol{\chi}_{\nu} \cdot \boldsymbol{M}$,[16] where $\boldsymbol{M}$ is the spontaneous or magnetic-field induced magnetization reflecting the conduction electron's spin polarization. The quantity $\boldsymbol{\chi}_{\nu} \cdot \boldsymbol{M}$, hereafter referred to as *magneto-chirality*, in the ordered longitudinal (Figure 1F) or transverse (Figure 1G) conical structures can cause the electronic-band asymmetry, even without relativistic SOC, which directly produces the nonreciprocal charge transport depending on the directions of current and $\boldsymbol{M}$.[15] To control the spin helicity in the proper screw structure (Figure 1E), for example, a dc current and a magnetic field causing $\boldsymbol{M}$ are simultaneously applied either parallel or antiparallel to stabilize the single-spin-helicity domains (magnetochiral (MCh)-poling). The nonreciprocal resistivity (NRR) due to the eMChE is used to detect the single or dominant spin helicity. Note here again that the eMChE due to the action of $\boldsymbol{\chi}_{\nu} \cdot \boldsymbol{M}$ does not require the relativistic SOC of the materials system.[16]

In this study, in addition to such an eMChE, we seek a new effect for control and detection of the spin helicity in a multiferroic conductor in terms of MP (magnetopolar) effect based on the SOC. The target magnetic structure is the transverse conical (TC) state (Figure 1G), in which $\boldsymbol{P}$ (electronic polarity) from cycloidal spin modulation and the net magnetization ($\boldsymbol{M} \perp \boldsymbol{P}$, $\boldsymbol{q}$) coexist, i.e., multiferroic.[17] For the switching of spin helicity or $\boldsymbol{P}$ direction in the TC state, we exploit the toroidal moment $\boldsymbol{T}$ which can couple with the current j; the toroidal moment is defined as $\boldsymbol{T} = \frac{1}{2} \sum_i \boldsymbol{r}_i \times \boldsymbol{S}_i$, where $\boldsymbol{r}_i$ and $\boldsymbol{S}_i$ are position and spin moment vectors at site i,[18] and hence in the multiferroic state is approximated as $\boldsymbol{T} \sim \boldsymbol{P} \times \boldsymbol{M}$ in the magnetically-ordered electrically-polar state (see Section S5, Supporting Information, for this justification). Combined with the expression of $\boldsymbol{P}$ in Equation (1), $\boldsymbol{T}$ in the general conical structure can be expressed as $\boldsymbol{T} \sim (\hat{\boldsymbol{q}} \times \boldsymbol{\chi}_{\nu}) \times \boldsymbol{M}$ with $\hat{\boldsymbol{q}}$ being the unit vector along the spin modulation $\boldsymbol{q}$ vector. This should show a distinct $\boldsymbol{M}$-directional dependence from the case of the magneto-chirality $\boldsymbol{\chi}_{\nu} \cdot \boldsymbol{M}$. Here, we report that the multiferroic state (TC state) in a conducting magnet YMn_6Sn_6 can be controlled electrically via such an MP effect of $\boldsymbol{T}$ as well. We call this effect the electrical magneto-toroidal effect (eMToE), which is distinct from eMChE. Moreover, the controlled multiferroic state is detected through a novel NRR arising from this eMToE as well as from the eMChE.

2. Result

2.1. Helimagnetic Orders of YMn_6Sn_6

The single crystal of YMn_6Sn_6 has a centrosymmetric hexagonal structure (space group $P6/mmm$, No. 191) with $a = b = 0.554$ nm and $c = 0.901$ nm (Figure 1A). The frustrated exchange interactions between $3d$ moments of Mn kagome lattices produce rich magnetic phase diagrams with some helical magnetic structures with the $\boldsymbol{q}$ vector along the c-axis (Figure 1C,D).[19–22] The intralayer exchange interaction is ferromagnetic, realizing easy-plane magnetic anisotropy. On the other hand, there are interlayer interactions, ferromagnetic and antiferromagnetic, between the two kinds of nearest-neighbor Mn-plane spins, which stabilizes an up-up-down-down like double-antiferromagnetic structure. In addition, the second-nearest-neighbor ferromagnetic interaction between the Mn-plane spins along the c-axis gives a frustration to this hypothetical commensurate order and stabilizes helical magnetic structures. Thus, the helix in this material has a distorted or a double helix structure, with two different spin rotation angles.[23] In the single helix structure, the angle between nearest-neighbor Mn-plane spins (α) become half of that between second-nearest-neighbor spins (β), i.e., $\alpha/\beta = 0.5$. On the other hand, in the double helix structure of YMn_6Sn_6, the ratio is $\alpha/\beta \sim 0.4$. The helical pitch is short in this material, ≈ 3 nm. The proper screw (PS) magnetic structure (Figure 1E) stabilizes in zero field over a wide range of temperatures between the lowest temperature (<2 K) and $T_N = 330$ K. Upon increasing the magnetic field applied along the c-axis, PS becomes the longitudinal conical (LC) structure (Figure 1F) because of tilt of spins along the magnetic field. The LC finally transforms into the forcedly ferromagnetic (FF) phase (Figure 1I) above a threshold magnetic field. On the other hand, with applying the magnetic field along the a-axis, a spin flop transition from the PS to the transverse conical (TC) structure (Figure 1G) occurs at around $B = 2.5$ T, where the spin rotation plane flops its direction by 90 degrees, i.e., from the ab-plane to the a^*c-plane; here a^* is set perpendicular to the a-axis within the ab-plane. These helical magnetic structures, PS, LC, and TC states, show the spin-helicity degree of freedom in the originally centrosymmetric chemical lattice. Aside from these helical magnetic structures, there is a fan-like (FL) phase (Figure 1H) above 7 T below 150 K. Just below the phase boundary at T_N, a mixture of antiferromagnetic order (AF) and PS, LC, or TC structure is observed.[23–27] The temperature dependence of the longitudinal resistivity along the c-axis is measured in 0 T and 5 T ($\boldsymbol{B}//a$) (Figure 1B), showing a low residual resistivity (<10 mΩ cm) and good metallicity. The kinks at 300 K and 270 K in the 5 T curve correspond to the FF-AF and AF-TC phase transitions.

Figure 1E–G further elaborates the magnetic structure of PS, LC, and TC phases along with the definition of spin helicity. (Hereafter, the actual double helix structure is approximated by the single helix presentation, which does not essentially change the following discussion of the results (see Section S4, Supporting Information, for this justification).) In the PS and LC structures, the rotation plane of the magnetic moment is perpendicular to the $\boldsymbol{q}$ vector ($//c$). The spin helicity is defined as right-handed or left-handed, depending on the direction of spin rotation viewed along the $\boldsymbol{q}$ vector. On the other hand, the external magnetic field (>2.5 T) applied perpendicular to the $\boldsymbol{q}$ vector stabilizes the TC, in which the rotation plane is parallel to the $\boldsymbol{q}$ vector. The spin helicity is defined as clockwise (CW) or counterclockwise (CCW), depending on the direction of the spin rotation of the cycloidal component viewed along the cone-axis of TC in proceeding along the $\boldsymbol{q}$ vector ($//c$). Without any procedure to create the single-spin-helicity domain using the current application, PS

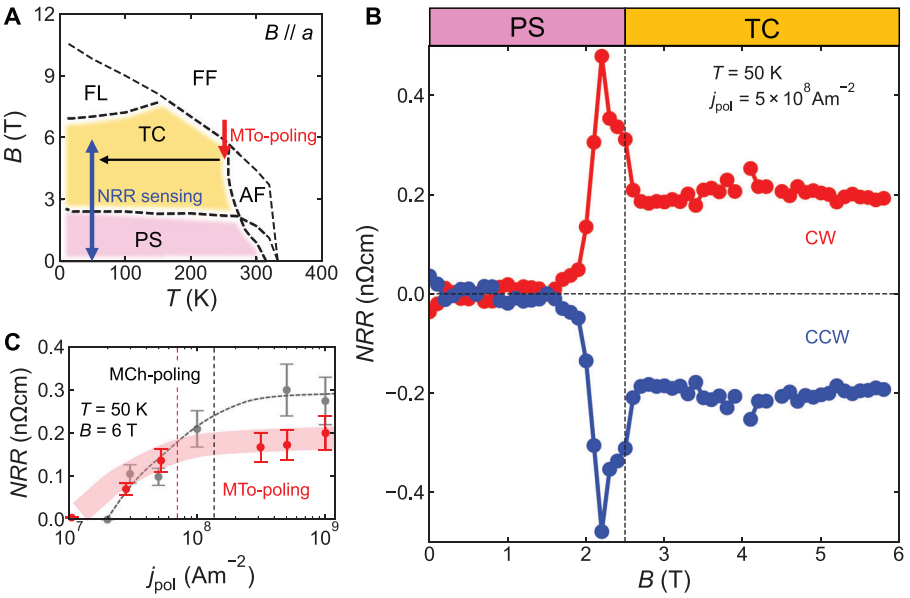

Figure 2. Control and detection of spin helicity in multiferroic transverse conical phase in YMn_6Sn_6. A) Magneto-toroidal (MTo)-poling (red arrow) and nonreciprocal resistivity (NRR) sensing (blue arrow) procedures are indicated in the magnetic phase diagram. B) Magnetic field dependence of the NRR measured at 50 K with $j_{ac} = 5 \times 10^8$ Am^{-2} after MTo-poling with $j_{pol} = +5 \times 10^8$ Am^{-2} (red, CW) and $j_{pol} = -5 \times 10^8$ Am^{-2} (blue, CCW). C) Poling current density j_{pol} dependence of NRR for MTo-poling (red) and mangetochiral (MCh)-poling (gray). The red and black vertical lines approximately indicate the threshold j_{pol}^{th} for MTo (for TC) and MCh (for LC) configurations, respectively. The red fat line and the gray dashed curve are the guides to the eyes.

and TC structures in YMn_6Sn_6 take the multi-domains of spin helicity with the nearly equal population due to the energetical degeneracy of the two spin-helicity states, as evidenced by almost indiscernible NRR behavior, *vide infra*.

One distinct feature in the TC phase is the existence of finite $\boldsymbol{P}$ as described by Equation (1), i.e., multiferroic in nature. Note that the direction of $\boldsymbol{P}$ is determined by the spin helicity of the cycloidal component of TC, i.e., CW or CCW. Moreover, TC has the magnetization component ($\boldsymbol{M}$) along the cone-axis, which is perpendicular to both $\boldsymbol{P}$ and $\boldsymbol{q}$ vectors. The toroidal moment $\boldsymbol{T} \sim \boldsymbol{P} \times \boldsymbol{M} \sim (\hat{\boldsymbol{q}} \times \boldsymbol{\chi}_v) \times \boldsymbol{M}$ is along the $\boldsymbol{q}$ vector (//c), and the sign of $\boldsymbol{T}$ is determined by the sign (CW or CCW) of spin helicity, or equivalently of $\boldsymbol{P}$, when $\boldsymbol{M}$ is fixed (Figure 1G). $\boldsymbol{T}$ can be viewed as a built-in vector potential $\boldsymbol{A}_{\text{eff}}$ under the SOC since the effective SOC term in Hamiltonian is described as

$$\lambda \boldsymbol{L} \cdot \boldsymbol{S} = \lambda (\boldsymbol{r} \times \boldsymbol{p}) \cdot \boldsymbol{S} = -\lambda (\boldsymbol{r} \times \boldsymbol{S}) \cdot \boldsymbol{p} = e\boldsymbol{A}_{\text{eff}} \cdot \boldsymbol{p} \quad (2)$$

where λ, $\boldsymbol{L}$, e, and $\boldsymbol{p}$ are the spin-orbit interaction, the angular momentum, and the electron's elementary charge and momentum, respectively.[28] Such $\boldsymbol{P}$ is generally small, but the resultant $\boldsymbol{T}$ can often have a significant effect on the electronic system, as shown in various nonlinear nonreciprocal optical effects even in a conducting state.[1,28,29] Note that, unlike the TC phase, the PS or LC phase configurations do not have finite $\boldsymbol{P}$ or $\boldsymbol{T}$ according to Equation (1).

2.2. Magneto-Toroidal Poling of Spin Helicity

In this study, we exploit the toroidal moment along the $\boldsymbol{q}$ vector (T_z) in the TC phase to control and detect the spin helicity. Note that only the z-axis component of $\boldsymbol{T}$ couples with the electric current flowing along the $\boldsymbol{q}$ (//z) vector in this experiment. $\boldsymbol{T}$ as a built-in vector potential couples with the electron's momentum $\boldsymbol{p}$ or electric current (Equation (2)). This means that the electronic-band asymmetry with respect to the k_z direction should arise in the TC phase, in a manner depending on the sign of the spin helicity or $\boldsymbol{P}$, and accordingly shows the nonreciprocal electron transport as determined by the sign of T_z, as shown in Figure 1J. Conversely, the electric current can align T_z and hence $\boldsymbol{P}$ and spin helicity in the case of a multi-helicity domain state. This MP coupling between the current and the spin helicity is analogous to the action of magneto-chirality $\boldsymbol{\chi}_v \cdot \boldsymbol{M}$, which are both expected to cause the electronic-band asymmetry. However, the former (latter) is relevant (irrelevant) to the relativistic SOC, and the $\boldsymbol{M}$-directional dependence is distinct from each other.

The current-induced poling of the ferrotoroidic domain was previously demonstrated for an antiferromagnet with a finite toroidal moment.[30] In a similar manner, it is expected that T_z in the present multiferroics with the ordered TC structure can also be switched by electric current density (j). We adopted a new procedure to control the spin helicity with such a T_z-j coupling mechanism as the working hypothesis, as termed *magneto-toroidal* (MTo)-*poling*. As shown in **Figure 2A**, at first, we applied the magnetic field along the a-axis (perpendicular to the $\boldsymbol{q}$//c) up to +7 T at 250 K, and the high dc current density j_{pol} along the c-axis. Here, j_{pol} in the opposite direction is anticipated to realize the opposite helicity of the TC phase in the end. We *tentatively* define the spin helicity of TC as CW and CCW after the MTo-poling with positive and negative j_{pol}, respectively. (We can know whether the spin helicity is reversed or not between CW and CCW, but cannot distinguish which is CW or CCW from the present nonlinear transport experiment alone, since the sign of

T_z and/or $\chi_\nu \cdot \boldsymbol{M}$ of CW or CCW depends on the material parameters, such as the coefficient A in Equation (1)) Then, the magnetic field was slowly removed at a reduction rate of 1.2 mTs^{-1} from 7 to 5 T while the current of j_{pol} was kept flowing, enabling to traverse the phase boundary from the FF phase into the TC phase (Figure 2A). Note that the FF phase does not have spin helicity, while the TC phase does. Traversing such a boundary from nonchiral to chiral magnetic phase is essential for the poling procedure. The MTo-poling is performed at a high temperature at 250 K to effectively reduce the energy barrier to switch the domains.

The spin helicity of the TC state is detected by the nonreciprocal charge transport arising from T_z and/or $\chi_\nu \cdot \boldsymbol{M}$. The sign of the NRR changes depending on the sign of T_z and/or $\chi_\nu \cdot \boldsymbol{M}$. Here the NRR is defined as an additional term ($\rho_{ch}j$) in the resistivity, up to the first order of j,

$$\rho(j) = \rho_0 + \rho_{ch} j \tag{3}$$

where ρ_0 and ρ_{ch} are linear resistivity and constant related to NRR, respectively. The NRR can be measured as a second harmonic (2ω) resistivity in the lock-in measurement while applying the ac current ($j = j_{ac}\sin(\omega t)$) with frequency of $f = \omega/2\pi$,

$$-\rho_{ch} j_{ac} \cos(2\omega t) = \rho^{2f} \cos(2\omega t) \tag{4}$$

The NRR refers to ρ^{2f}. The NRR signal is finite when T_z and/or $\chi_\nu \cdot \boldsymbol{M}$ is finite. Therefore, the single spin helicity realized by the MTo-poling can be detected by the finite NRR in the TC phase which becomes saturated as increasing j_{pol}. Hereafter, we call this method *NRR sensing*. As illustrated in Figure 2A, the NRR sensing was performed at 50 K after the MTo-poling at 250 K. Once the MTo-poling was completed at 250 K, the system was cooled down to 50 K in 5 T. Then, the field was raised up to 6 T, which is just below the phase boundary between TC and FL (see Figure 1C). The NRR was measured while the field was swept between 6 and 0 T. During the field sweep, ac electric current with $j_{ac} = 5 \times 10^8$ Am^{-2} and $f = 1$ kHz was applied along the c-axis, as a probe excitation to detect the NRR. We first focus on the NRR sensing at 50 K, where the temperature is low enough to ensure the well-ordered helical states with robustly fixed spin helicity. At the same time, 50 K is high enough to ignore the effect of the possible Joule heating from the application of large current density.

Figure 2B shows the representative result of the NRR sensing after MTo-poling with $j_{pol} = \pm 5 \times 10^8$ Am^{-2}. To correct some background extrinsic contributions to nonreciprocal signals, we defined the extrinsic background as an average of CW ($+j_{pol}$) and CCW ($-j_{pol}$) signals, and then we derived the NRR for $\pm j_{pol}$ as deviations from this background level; see Section S1 (Supporting Information) for the detailed procedure of data analysis and its justification. (Thus, the CW and CCW NRRs shown in the figures show up as plus-minus symmetric curves by definition.) At the beginning of the field sweep from 6 T, the system is in the TC phase, and the NRR is finite at ≈+0.2 and −0.2 nΩ cm for CW and CCW states, respectively. The magnitude of the signal keeps its value until the system undergoes the phase transition at 2.5 T to the PS phase. The NRR value is confirmed to be linear to the probe ac current density j_{ac} as expected from Equation (4) (see Section S2, Supporting Information). After the phase transition into the PS phase is completed with the decrease of the magnetic field, the NRR becomes nearly zero. This is consistent with the expectation that T_z and $\chi_\nu \cdot \boldsymbol{M}$ are finite in the TC phase but both are zero in the PS phase. (Note that $\chi_\nu \cdot \boldsymbol{M}$ is also zero in the present case since $\chi_\nu \perp \boldsymbol{M}$ in the PS phase with $\boldsymbol{M}//x$.) In the course of the TC-to-PS transition, however, a large sharp peak structure of NRR is observed immediately below the phase boundary at 2.5 T, which may arise from the effect of asymmetric charge-carrier scattering on the residual or fluctuating chiral spin clusters in the PS phase close to the boundary with the TC phase.[16] This NRR response is distinct in the mechanism from the NRR in the long-range ordered TC phase and will be elaborated in the following section.

Figure 2C shows the j_{pol} dependence of the magnitude of NRR. With small $j_{pol} = 1 \times 10^7$ Am^{-2}, the NRR in the TC phase is not discerned (see Figure S1D, Supporting Information), showing that the multi-domains of spin helicity with the nearly equal population of the CW and CCW states. Upon increasing the j_{pol}, the magnitude of NRR increases and then saturates at around $j_{pol}^{th} = 7 \times 10^7$ Am^{-2}. The threshold or lower limit of j_{pol} indicates the existence of a small energy barrier left between CW and CCW states, even during the poling procedure through the phase boundary, which is perhaps due to some pinning centers of the domains or domain walls from impurities and structural disorder. The saturation of the NRR indicates that the single-helicity domain is realized above the j_{pol}^{th}. Thus, the MTo-poling and the NRR sensing using the toroidal moment T_z and/or the magnetochirality $\chi_\nu \cdot \boldsymbol{M}$ are shown to be applicable to control and detect the spin helicity in the multiferroic TC metal state. As for the spin-helicity control of the PS or LC phase, the MCh-poling, which can be done via poling under the current flow and the external magnetic field both along the $\boldsymbol{q}$ direction (c-axis), is effective as shown in previous studies,[11,12] while the T_z-based MTo-poling is not applicable for the LC phase. In fact, we could achieve similar MCh-poling and NRR sensing of the PS/LC phase, as described in Section S3 (Supporting Information). Figure 2C is also shown the j_{pol} dependence of the magnitude of NRR for the MCh-poling; the j_{pol}^{th} in this case is ≈1×10^8 Am^{-2}, appreciably larger than the case of the MTo-poling, while the saturated NRR value is larger, implying that the microscopic poling mechanism is more or less different between the MTo- and MCh- poling as anticipated.

2.3. Angular Dependence of NRR

The NRR sensing is performed in various magnetic field sweep directions after the MTo-poling, to establish the relative contribution of the above two distinct mechanisms, i.e., based on T_z and $\chi_\nu \cdot \boldsymbol{M}$, to the NRR in TC phase. The magnetic field is swept from 0 to 6 T at various deviation angles θ from the a-axis within the ac-plane, as shown in the left panel of **Figure 3A**: $\theta = 0°$ corresponds to the limit where T_z takes the maximum, and $\theta = 90°$ to the limit where T_z is zero. The NRR of the T_z origin is termed the electrical magneto-toroidal effect (eMToE).[31] At $\theta = 0°$, the NRR is from both finite T_z and $\chi_\nu \cdot \boldsymbol{M}$ in the TC phase. On the other hand, at $\theta = 90°$, where $T_z = 0$, the NRR arises solely from the eMChE in the LC phase. At angles in between, the NRR may appear from both of these effects. With increasing θ from 0°, the NRR in the low-field region below 2 T gradually

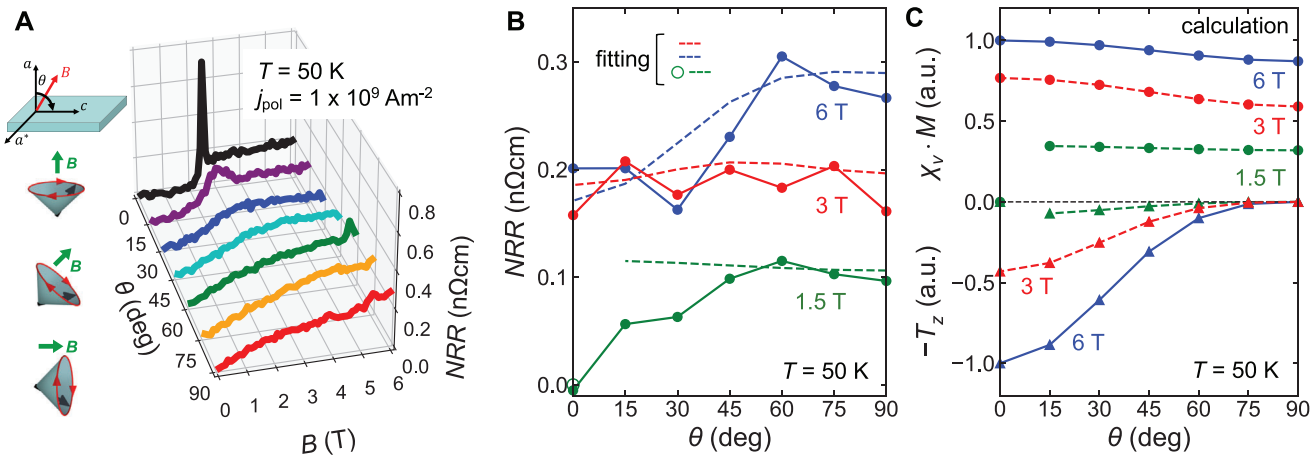

Figure 3. Angular dependence of nonreciprocal resistivity (NRR). A) Magnetic field dependence of NRR under various magnetic field directions within the *ac*-plane. The NRR sensing is performed at 50 K in various magnetic field directions with $j_{ac} = 5 \times 10^8$ Am^{-2} after MTo-poling with $j_{pol} = 1 \times 10^9$ Am^{-2}. Schematics show the definition of the magnetic field rotation angle θ, and the cone-axis directions in TC phase at $\theta = 0°$ ($\boldsymbol{B}//a$), 45° and 90° ($\boldsymbol{B}//c$). B) θ dependence of NRR in 6 T (blue), 3 T (red) and 1.5 T (green) at 50 K. Blue, red and green dashed lines are the fitting by the superposition of the calculated magneto-chirality $\chi_\nu \cdot \boldsymbol{M} = (\boldsymbol{S}_i \times \boldsymbol{S}_j) \cdot \boldsymbol{M}$ and the toroidal moment along the $\boldsymbol{q}$ vector $T_z \sim [(\hat{\boldsymbol{q}} \times \chi_\nu) \times \boldsymbol{M}]z$ in C). (See the main text for the details.) The fitting for 1.5 T data is difficult due to the PS-LC spin flop transition at low θ region and hence tentatively shown between $\theta = 15°$ and 90°. Fitting for $\theta = 0°$ is shown separately with the green open circle. C) Calculated θ dependence of $\chi_\nu \cdot \boldsymbol{M}$ and T_z at 50 K. Blue, red, and green correspond to the values in 6, 3, and 1.5 T, respectively.

increases toward the peak structure at ≈2.5 T. The peak structure at $\theta = 15°$ is not as sharp as compared to that at $\theta = 0°$ where the PS-TC spin flop transition is well-defined. Upon increasing the tilt angle, the peak structure becomes even duller toward $\theta = 30°$ and the NRR increases almost monotonically at angles $\theta \geqq 45°$.

The observed NRR magnitudes at 50 K and at selected values of magnetic field $B = 1.5$, 3, and 6 T are plotted in Figure 3B as a function of the angle θ of $\boldsymbol{B}$ from the *a*-axis. The respective behaviors are predicted by a simple calculation (see Section S4, Supporting Information) of the angular dependence of $\chi_\nu \cdot \boldsymbol{M}$ and $T_z \sim [(\hat{\boldsymbol{q}} \times \chi_\nu) \times \boldsymbol{M}]z$, as shown in Figure 3C. Among these, $\chi_\nu \cdot \boldsymbol{M}$ does not have strong angular dependence at 3 and 6 T in the course of TC-to-LC phase change, where the spin cone-axis continuously rotates in the ac plane as schematically shown in the left panel of Figure 3A. However, $\chi_\nu \cdot \boldsymbol{M}$ at 1.5 T is zero in the genuine PS phase at $\theta = 0°$ (see Figure 1C) and gradually increases with θ toward the LC state (see Figure 1D). This behavior depends on the critical field strength for the spin flop transition at general θ (2.5 T at $\theta = 0°$) which is not easily estimated. Therefore, the continuous rotation of the cone-axis is tentatively assumed also in the calculation at 1.5 T between $\theta = 15°$ and 90°. On the contrary, T_z is strongly suppressed toward $\theta = 90°$ from its maximum value at $\theta = 0°$ (Figure 3C). T_z appears almost doubled with B changing from 3 T to 6 T, while T_z in 1.5 T is zero in the PS phase ($\theta = 0°$). For angles between $\theta = 15°$ and 90°, T_z is again calculated assuming the continuous cone-axis rotation and vanishingly small values are obtained due to the large cone-opening angle at 1.5 T. The angular dependence of the NRR in 3 and 6 T (all the cases where the contribution from the spin-cluster scattering is small enough) are fit by the superposition of these two amounts ($NRR = a\chi_\nu \cdot \boldsymbol{M} + bT_z$) as shown in Figure 3B. The coefficients are found to be $a = 0.33$ and $b = -0.16$, indicating the opposite-sign contribution from $\chi_\nu \cdot \boldsymbol{M}$ and T_z with the comparable absolute magnitude, approximately, 2:1. In this way, the eMChE and eMToE can be separably estimated. In particular, the NRR in the TC phase of YMn_6Sn_6 partly arises from a newly assigned mechanism, namely eMToE based on SOC, which is different in origin from the conventional eMChE observed in the LC phase. Note that the sign of the resultant NRR in the present case is more dominated by eMChE than by eMToE, however, the situation will depend on the actual materials parameters for the TC phase, in particular on the magnitude of the relativistic SOC favoring the eMToE.

2.4. Enhancement of NRR by Spin-Cluster Scattering at Phase Boundaries

The observed NRR phenomena in the helimagnetically ordered phases of PS and TC, the NRR appears to arise from the electronic-band dispersion asymmetry between $+k_z$ and $-k_z$ due to the presence of T_z and/or $\chi_\nu \cdot \boldsymbol{M}$; here z is the axis along the helical $\boldsymbol{q}$-vector ($//c$). Apart from these NRR signals in the ordered phases, the conspicuous NRR scattering peak structure is observed at the PS-TC phase boundary, as shown in Figure 2B. We assign this conspicuous NRR peak not to the electronic-band dispersion asymmetry effect but to the nonreciprocal scattering from the spin cluster with the vector spin chirality $\chi_\nu = \boldsymbol{S}_i \times \boldsymbol{S}_j$,[16] embedded in the paramagnetic or non-NRR ordered phase (e.g., the PS phase). Such a scattering-effect NRR signal was typically observed for a chiral magnet MnSi near above the helical magnetic transition temperature under a magnetic field.[32] **Figure 4A** shows the NRR response in a whole magnetic field region of 0–14 T for $\boldsymbol{B}//a$ ($\theta = 0°$). It is worth noting that the spin-cluster scattering seems to occur at the respective phase boundaries, not only at PS-TC but also at FL-FF boundaries, and that the memory effect of spin helicity subsists even in the FF phase, as follows: The

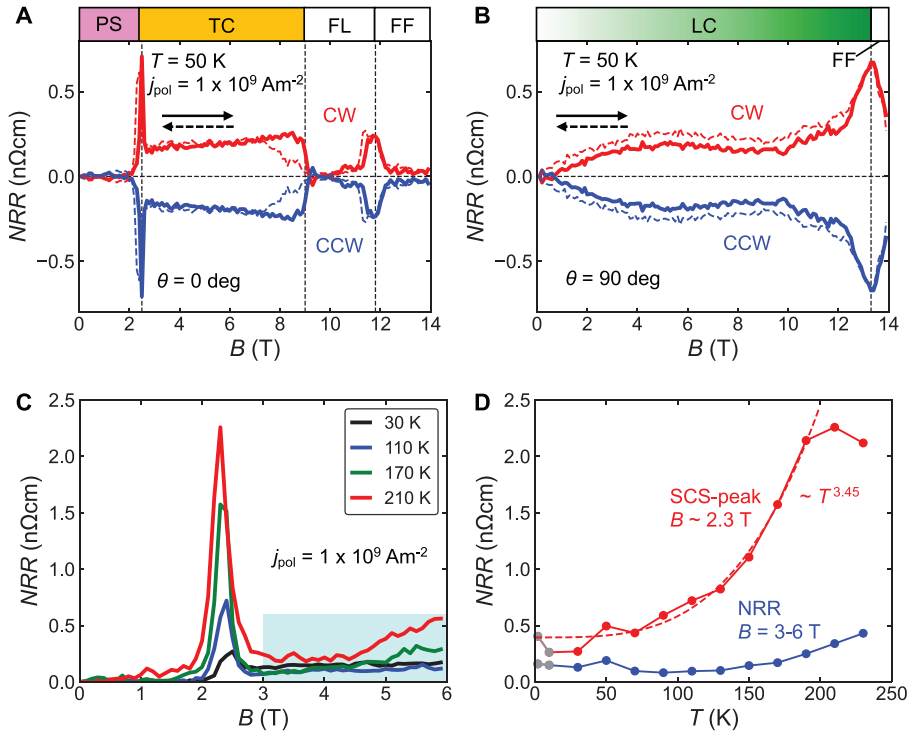

Figure 4. Enhancement of nonreciprocal resistivity (NRR) at phase boundaries. Magnetic field dependence of NRR up to 14 T at A) $\theta = 0°$ and B) $\theta = 90°$ measured at 50 K with $j_{ac} = 5 \times 10^8$ Am^{-2} after MTo-poling with $j_{pol} = +1 \times 10^9$ Am^{-2} (red, CW) and $j_{pol} = -1 \times 10^9$ Am^{-2} (blue, CCW), respectively. Solid and dashed lines indicate the upward and downward magnetic field sweep directions, respectively. The upward sweeps are performed first just after the MTo-poling procedures. C) Magnetic field ($\boldsymbol{B}//a$) dependence of NRR measured at various temperatures with $j_{ac} = 5 \times 10^8$ Am^{-2} after MTo-poling with $j_{pol} = +1 \times 10^9$ Am^{-2}. D) Temperature dependence of NRR value at peak of spin-cluster scattering (SCS) at PS-TC phase boundary (red) and NRR value of electronic-band asymmetry origin in TC phase (blue). The red dashed line shows the fitting with $NRR = a + bT^n$ ($n = 3.45$). The data points shown in gray are not enough reliable due to the contribution from the Joule heating in the sample.

NRR is measured at 50 K after MTo-poling with $j_{pol} = \pm 1 \times 10^9$ Am^{-2}. The magnetic field ($\theta = 0°$) is first increased from 0 to 14 T, traversing the magnetic phases in the order of PS, TC, FL, and FF. Then, the field is decreased from 14 to 0 T. In the upward sweep, the NRR becomes finite after the sharp peak structure at 2.5 T until the TC-FL phase boundary at 9 T. Then, in the FL phase, where the spin helicity is not well-defined, the NRR takes nearly zero value. At the FL-FF phase boundary, however, the NRR again shows a spin-helicity dependent, i.e., poling-history dependent, peak. The FL and FF phases in the well-ordered state should not show NRR because of the non-chiral nature of the ordered spin moments. Near the phase boundary, however, the domain walls between FF and FL domains are anticipated to form with the noncollinear spins, i.e., vector spin chirality, and perhaps work as scattering centers of NRR. Interestingly, the memory of the spin helicity appears to be kept even in magnetic phases where the spin helicity appears not to be defined, i.e., FL and FF phases. The NRR is again approaching zero in the FF phase with a further increase of magnetic field. Surprisingly, the magnetic field dependence of the NRR in the downward sweep follows the nearly same curve as in the upward sweep. This may be because the spin helicity is memorized possibly by the thermal fluctuation of spins,[33] or the residual helical spin clusters even in the FL or the FF phases. A similar NRR peak of scattering origin is also observed for the phase boundary between LC and FF in the case of $\boldsymbol{B}//c$ ($\theta = 90°$), as shown in Figure 4B.

The sharp enhancement of NRR at the PS-TC phase boundary is further elaborated. Figure 4C shows the magnetic field dependence of the NRR measured at various temperatures after the MTo-poling. The temperature dependence of the peak value of the NRR (scattering term) at PS-TC phase boundary at $B = 2.5$ T and the magnitude of the NRR (electronic-band asymmetry term) in the long-range ordered TC phase averaged over 3–6 T are plotted in Figure 4D. The scattering peak value is conspicuously increased with the temperature and takes the maximum at 210 K. The large temperature effect of the NRR of scattering origin is due to the thermal spin fluctuation which contributes to the enhanced averaged value of the vector spin chirality $< \chi_\nu >$.[16,32] On the other hand, the NRR from eMToE and eMChE of the asymmetric band-dispersion origin in the long-range ordered TC phase is almost constant at low temperatures below 150 K, while slightly enhanced toward high temperature.

3. Conclusion

We have demonstrated the spin-helicity control and detection in a high-temperature helimagnet YMn_6Sn_6 in its multiferroic transverse conical (TC) phase in terms of the electrical magneto-toroidal effect (eMToE) based on the coupling between toroidal moment and electric current, in addition to the conventional electrical magnetochiral effect (eMChE). We utilized the NRR to detect the controlled spin helicity. In addition, the

thermally-enhanced large NRR is observed at the magnetic phase boundary between the proper screw (PS) and TC phases as well as between longitudinal conical (LC) and forced ferromagnetic (FF) phases, presumably due to the nonreciprocal scattering effect from the spin cluster with vector spin chirality. The spin-helicity control achieved in the TC phase means the control of the electronic polarity constituting the toroidal moment in the conductor as induced by the cycloidal spin order. Having shown that the spin-helicity control in a conductor is possible in the magneto-toroidal configuration, the scope of candidate materials for spintronics based on the spin-helicity degree of freedom is now expanded. For example, there is a possibility that one can control the spin helicity of nanometric skyrmions,[34] irrespective of Néel-wall type (cycloid) or Bloch-wall type (screw) even in originally centrosymmetric metallic materials,[35] in terms of the MTo- or MCh- poling, as shown here, without changing the chemical composition of a material,[36] or applying a strain.[37] In a broader perspective, the exploration of multiferroic conductors with control of emergent electronic polarity and toroidal moment would pave the way to new spintronic materials.

4. Experimental Section

Single Crystal Growth: Single crystals of YMn_6Sn_6 were synthesized by a Sn flux method.[20] A mixture of ingredient elements with a molar ratio of Y:Mn:Sn = 1:6:30 was put in an aluminum oxide crucible and then sealed in an evacuated quartz tube. The tube was heated up to 1050 °C, and subsequently cooled down slowly to 600 °C in an electric furnace. When the furnace reached 600 °C, excess flux was centrifuged. The obtained single crystals with well-developed facet structures were soaked in hydrochloric solution to remove remaining flux. The single crystallinity was confirmed by Laue X-ray diffraction. No impurity phase was detected by powder X-ray diffraction.

Focused Ion Beam (FIB) Device Fabrication: A thin plate (10 × 20 × 1 μm3) of the single crystal was cut out by using the focused ion beam (FIB) fabrication technique (NB-5000, Hitachi). The plate was mounted on a silicon substrate with patterned Au/Ti-bilayer electrodes. The plate was electrically connected to the electrodes by FIB-assisted tungsten deposition. The plate was finally fabricated into a Hall-bar shape.

Transport Measurements: The control and detection of spin helicity were performed in the Physical Property Measurement System (PPMS, Quantum Design). dc electric current was applied to the FIB device through a current source (K6221, Keithley) during the MTo- and MCh-poling procedure. The nonreciprocal resistivity (NRR) was measured by lock-in amplifiers (LI5660, NF corporation). ac current of 1 kHz was applied to detect the second harmonic resistivity. The voltage signal from the device was pre-amplified with a low-noise amplifier (SR560, Stanford Research Systems). For the details of the data processing, see Section S1 (Supporting Information).

Calculation of Magneto-Chirality and Toroidal Moment: The calculation of the magneto-chirality and the toroidal moment is performed using relevant data such as magnetization, modulation period of helical magnetic structure, and lattice constants extracted from the references.[25,27] See Section S4 (Supporting Information) for the detailed descriptions.

Supporting Information

Supporting Information is available from the Wiley Online Library or from the author.

Acknowledgements

The authors thank D. Nakamura and Y. Taguchi for fruitful discussions. This work was supported in part by JSPS KAKENHI (Grant No. 23H05431) and JST PRESTO (Grant No. JPMJPR23Q3). N.N. was supported by JSPS KAKENHI (Grant No. 24H00197 and No. 24H02231). N.N. was supported by the RIKEN TRIP initiative.

Conflict of Interest

The authors declare no conflict of interest.

Author Contributions

Y.T. conceived and supervised the project. D.Y. performed device fabrication, transport measurements, data analysis/visualization, and calculation. A.K. grew single crystals. D.Y. and Y.T. wrote the original draft. N.N. reviewed and edited the draft. All the authors discussed the results and commented on the manuscript.

Data Availability Statement

The data that support the findings of this study are available from the corresponding author upon reasonable request.

Keywords

high-temperature helimagnet, multiferroics of spin origin, spin-helicity control, spintronics, toroidal moment

Received: December 31, 2024
Revised: March 25, 2025
Published online: April 7, 2025

[1] Y. Tokura, S. Seki, N. Nagaosa, *Rep. Prog. Phys.* **2014**, *77*, 076501.
[2] H. Katsura, N. Nagaosa, A. V. Balatsky, *Phys. Rev. Lett.* **2005**, *95*, 057205.
[3] M. Mostovoy, *Phys. Rev. Lett.* **2006**, *96*, 067601.
[4] I. A. Sergienko, E. Dagotto, *Phys. Rev. B* **2006**, *73*, 094434.
[5] Y. Yamasaki, H. Sagayama, T. Goto, M. Matsuura, K. Hirota, T. Arima, Y. Tokura, *Phys. Rev. Lett.* **2007**, *98*, 147204.
[6] Y. Yamasaki, S. Miyasaka, Y. Kaneko, J.-P. He, T. Arima, Y. Tokura, *Phys. Rev. Lett.* **2006**, *96*, 207204.
[7] P. W. Anderson, E. I. Blount, *Phys. Rev. Lett.* **1965**, *14*, 217.
[8] S. Bhowal, N. A. Spaldin, *Annu. Rev. Mater. Res.* **2023**, *53*, 53.
[9] N. Nagaosa, *J. Phys. Soc. Jpn.* **2023**, *92*, 081002.
[10] N. T. Bechler, J. Masell, *Neuromorph. Comput. Eng.* **2023**, *3*, 034003.
[11] N. Jiang, Y. Nii, H. Arisawa, E. Saitoh, Y. Onose, *Nat. Commun.* **2014**, *11*, 1601.
[12] H. Masuda, T. Seki, J. Ohe, Y. Nii, H. Masuda, K. Takanashi, Y. Onose, *Nat. Commun.* **2024**, *15*, 1999.
[13] G. L. J. A. Rikken, J. Folling, P. Wyder, *Phys. Rev. Lett.* **2001**, *87*, 236602.
[14] F. Pop, P. Auban-Senzier, E. Canadell, G. L. J. A. Rikken, N. Avarvari, *Nat. Commun.* **2014**, *5*, 3757.
[15] D. Nakamura, M. K. Lee, K. Karube, M. Mochizuki, N. Nagaosa, Y. Tokura, Y. Taguchi, *arXiv:* **2024**, 241202272.
[16] H. Ishizuka, N. Nagaosa, *Nat. Commun.* **2020**, *11*, 2986.
[17] Y. Tokura, *Science* **2006**, *312*, 1481.
[18] N. A. Spaldin, M. Fiebig, M. Mostovoy, *J. Phys. Condens. Matter* **2008**, *20*, 434203.

[19] G. Venturini, D. Fruchart, B. Malaman, *J. Alloys Compd.* **1996**, *236*, 102.
[20] A. Matsuo, K. Suga, K. Kindo, L. Zhang, E. Brück, K. H. J. Buschow, F. R. de Boer, C. Lefèvre, G. Venturini, *J. Alloys Compd.* **2006**, *408–412*, 110.
[21] K. Uhlířová, V. Sechovský, F. R. de Boer, S. Yoshii, T. Yamamoto, M. Hagiwara, C. Lefèvre, G. Venturini, *J. Magn. Magn. Mater.* **2007**, *310*, 1747.
[22] A. A. Bykov, Y. O. Chetverikov, A. N. Pirogov, S. V. Grigor'ev, *JETP Lett.* **2015**, *101*, 699.
[23] A. Kitaori, J. S. White, N. Kanazawa, V. Ukleev, D. Singh, Y. Furukawa, T.-h. Arima, N. Nagaosa, Y. Tokura, *Phys. Rev. B* **2023**, *107*, 024406.
[24] N. J. Ghimire, R. L. Dally, L. Poudel, D. C. Jones, D. Michel, N. Thapa Magar, M. Blemel, M. A. McGuire, J. S. Jiang, J. F. Mitchell, J. W. Lynn, I. I. Mazin, *Sci. Adv.* **2020**, *6*, abe2680.
[25] Q. Wang, K. J. Neubauer, C. Duan, Q. Yin, S. Fujitsu, H. Hosono, F. Ye, R. Zhang, S. Chi, K. Krycka, H. Lei, P. Dai, *Phys. Rev. B* **2021**, *103*, 014416.
[26] H. Zhang, X. Feng, T. Heitmann, A. I. Kolesnikov, M. B. Stone, Y.-M. Lu, X. Ke, *Phys. Rev. B* **2020**, *101*, 100405(R).
[27] R. L. Dally, J. W. Lynn, N. J. Ghimire, D. Michel, P. Siegfried, I. I. Mazin, *Phys. Rev. B* **2021**, *103*, 094413.
[28] Y. Tokura, N. Nagaosa, *Nat. Commun.* **2018**, *9*, 3740.
[29] C. Tzschaschel, J.-X. Qiu, X.-J. Gao, H.-C. Li, C. Guo, H.-Y. Yang, C.-P. Zhang, Y.-M. Xie, Y.-F. Liu, A. Gao, D. Bérubé, T. Dinh, S.-C. Ho, Y. Fang, F. Huang, J. Nordlander, Q. Ma, F. Tafti, P. J. W. Moll, K. T. Law, S.-Y. Xu, *Nat. Commun.* **2024**, *15*, 3017.
[30] P. Wadley, B. Howells, J. Železný, C. Andrews, V. Hills, R. P. Campion, V. Novák, K. Olejník, F. Maccherozzi, S. S. Dhesi, S. Y. Martin, T. Wagner, J. Wunderlich, F. Freimuth, Y. Mokrousov, J. Kuneš, J. S. Chauhan, M. J. Grzybowski, A. W. Rushforth, K. W. Edmonds, B. L. Gallagher, T. Jungwirth, *Science* **2016**, *351*, 587.
[31] H. Isobe, N. Nagaosa, *J. Phys. Soc. Jpn.* **2022**, *91*, 115001.
[32] T. Yokouchi, N. Kanazawa, A. Kikkawa, D. Morikawa, K. Shibata, T. Arima, Y. Taguchi, F. Kagawa, Y. Tokura, *Nat. Commun.* **2017**, *8*, 866.
[33] S. Onoda, N. Nagaosa, *Phys. Rev. Lett.* **2007**, *99*, 027206.
[34] N. Nagaosa, Y. Tokura, *Nat. Nanotechnol.* **2013**, *8*, 899.
[35] Y. Tokura, N. Kanazawa, *Chem. Rev.* **2021**, *121*, 2857.
[36] K. Shibata, X. Z. Yu, T. Hara, D. Morikawa, N. Kanazawa, K. Kimoto, S. Ishiwata, Y. Matsui, Y. Tokura, *Nat. Nanotechnol.* **2013**, *8*, 723.
[37] Y. Liu, B. Yang, X. Guo, S. Picozzi, Y. Yan, *Phys. Rev. B* **2024**, *109*, 094431.
[38] K. Momma, F. Izumi, *J. Appl. Cryst.* **2011**, *44*, 1272.